COMMUNICATION

ADVANCED
MATERIALS
www.advmat.d
Check for updates

Promoted Photocharge Separation in 2D Lateral Epitaxial Heterostructure for Visible-Light-Driven CO_2 Photoreduction

Li Wang,* Xue Zhao, Dongdong Lv, Chuangwei Liu, Weihong Lai, Chunyi Sun,* Zhongmin Su, Xun Xu, Weichang Hao, Shi Xue Dou, and Yi Du*

Photocarrier recombination remains a big barrier for the improvement of solar energy conversion efficiency. For 2D materials, construction of heterostructures represents an efficient strategy to promote photoexcited carrier separation via an internal electric field at the heterointerface. However, due to the difficulty in seeking two components with suitable crystal lattice mismatch, most of the current 2D heterostructures are vertical heterostructures and the exploration of 2D lateral heterostructures is scarce and limited. Here, lateral epitaxial heterostructures of $BiOCl@Bi_2O_3$ at the atomic level are fabricated via sonicating-assisted etching of Cl in BiOCl. This unique lateral heterostructure expedites photoexcited charge separation and transportation through the internal electric field induced by chemical bonding at the lateral interface. As a result, the lateral $BiOCl@Bi_2O_3$ heterostructure demonstrates superior CO_2 photoreduction properties with a CO yield rate of about 30 µmol g^{-1} h^{-1} under visible light illumination. The strategy to fabricate lateral epitaxial heterostructures in this work is expected to provide inspiration for preparing other 2D lateral heterostructures used in optoelectronic devices, energy conversion, and storage fields.

Solar energy is a green and renewable energy source.[1,2] It can be converted into electricity via solar cell or be stored into chemical forms via photocatalytic water splitting for H_2 and photocatalytic CO_2 reduction for CO, CH_4, etc.[3–7] As a result, employing solar energy is recognized as a promising strategy to meet continuously increased worldwide energy demand. The typical

solar-energy conversion process, not only in solar cell but also in photocatalysis, involves solar-light harvesting and photoexcited charge carrier separation/transportation.[8,9] Heterostructure, in which materials with different properties are integrated together, generally can harvest wide solar light derived from multiple components and possesses prominent photoexcited charge separation/transportation properties benefiting from internal electric field formed at the heterointerface.[10] Hence, exploring suitable components to construct heterostructure represents an efficient and facile strategy to improve the solar energy conversion efficiency.

Nowadays, 2D materials have attracted enormous research interest in optical electronic devices, catalysis, and solar-energy conversion fields due to their high specific surface area,[11] large fraction of surface exposed atoms,[12] and excellent mechanical, optical, and electronic properties.[13,14] Benefiting from layered structural properties, 2D materials are prone to be constructed into heterostructures. Typically, 2D heterostructures include vertical heterostructures in which the layers of various 2D materials are stacked vertically,[15] and lateral heterostructures in which multiple 2D materials are seamlessly stitched lateral.[16] Most of the current reported 2D heterostructures

Dr. L. Wang, Dr. W. Lai, Dr. X. Xu, Prof. S. X. Dou, Prof. Y. Du
Institute for Superconducting and Electronic Materials (ISEM)
Australian Institute for Innovative Materials (AIIM)
University of Wollongong
Wollongong, New South Wales 2500, Australia
E-mail: yi_du@uow.edu.au
Dr. L. Wang
Chair for Photonics and Optoelectronics
Nano-Institute Munich
Ludwig-Maximilians-Universität München
Königinstr. 10, Munich 80539, Germany
E-mail: li.wang@lmu.de

X. Zhao, Prof. C. Sun, Prof. Z. Su
Department of Chemistry
Northeast Normal University
Changchun, Jilin 130024, P. R. China
E-mail: suncy009@nenu.edu.cn
Dr. D. Lv, Dr. X. Xu, Prof. W. Hao, Prof. Y. Du
BUAA-UOW Joint Research Centre and School of Physics
Beihang University
Beijing 100191, P. R. China
Dr. C. Liu
Department of Energy Conversion and Storage
Technical University of Denmark
Lyngby 2800, Denmark

are vertical heterostructures, such as $BiOI/Bi_2WO_6$, $Bi_{12}O_{17}Cl_2/MoS_2$. In vertical heterostructures, the internal electric field at the heterointerface is originated from the van der Waals force between interlayers.[8,17–19] As is known, the van der Waals force is weaker than chemical bonding which exists at heterointerface in lateral heterostructures. Thus, the photoexcited charge separation/transportation properties are proposed to be better in lateral heterostructure. However, due to strict restrictions in lattice mismatch and difficulties in selecting suitable components, the construction of lateral heterostructures is strictly limited to few species. Hence, exploring the possibilities of new 2D lateral heterostructures is of great importance to promote the evolution of materials and improve the solar-energy conversion efficiency.

Bismuth oxyhalides (BiOX, X = Cl, Br, I) represent a popular species of 2D semiconductors due to their special *sp* hybridization which results in photogenerated charge carriers with less effective mass and superior mobility.[4,19] In the typical crystal structure of BiOX, $[Bi_2O_2]^{2+}$ layer is sandwiched between two slabs of halogen ions by strong electrovalent bonds along the highly active [001] direction, and the two neighboring slabs of halogen ions are connected by van de Waals interactions.[20,21] Benefiting from this unique structure, Bi_2O_3, which is a typical visible-light sensitizer, has the inherent priority to be in situ formed in BiOCl via removing halogen ions in the interlayer. In this work, $BiOCl@Bi_2O_3$ with lateral epitaxial heterostructure is fabricated via etching the edged halogen ion of BiOCl with the assistance of Ag and water molecule under sonicating. It is proved that $BiOCl@Bi_2O_3$ can not only take the advantages of both BiOCl and Bi_2O_3 in solar absorption but also can delocalize the photoproduced charge carriers via in-building driving force generated by lateral heterojunction. As a result, the lateral heterogeneous $BiOCl@Bi_2O_3$ possesses great potential to be excellent photocatalyst, and its CO yield rate for the CO_2 photoreduction process under visible light irradiation is about 30 μmol g^{-1} h^{-1}. This facile method to prepare lateral heterostructure paves way to fabricate other 2D lateral

heterostructure, and thus facilitates their further application in electronic devices, energy storage, and conversion fields.

As observed in our previous work, Ag nanoparticles are prone to be loaded on the edge of BiOCl during the hydrothermal reaction under the perturbation of water with the content close to 10%.[4] With the content of water continuously increasing to be larger than 20%, the edge of BiOCl starts to be etched into multiple layered thin nanosheets of Bi_2O_3 by the loaded Ag nanoparticles. Interestingly, the dimension of the generated thin nanosheets increases with the content of water increasing. The fabrication process and the proposed formation mechanism of $BiOCl@Bi_2O_3$ with lateral epitaxial heterostructure are illustrated in **Figure 1** and Figure S1, Supporting Information. The SEM images of $BiOCl-Ag-Bi_2O_3$ composites with different content of water involved are displayed in Figures S2–S7, Supporting Information. As demonstrated in Figure S2, Supporting Information, Ag is loaded on the surface of BiOCl when BiOCl is retreated with Ag nanoparticles and pure ethanol via hydrothermal method, indicating that $BiOCl–Bi_2O_3$ cannot be fabricated without the assistance of water. To investigate the role of Ag in the fabrication process of $BiOCl–Bi_2O_3$, BiOCl retreated with pure water via hydrothermal method is carried out. The SEM image in Figure S8, Supporting Information, and the UV–vis diffuse reflectance spectrum in Figure S9, Supporting Information, show that no big difference appears on the morphology and composition of BiOCl after retreated with pure water. It reveals that the only water cannot induce the growth of $BiOCl–Bi_2O_3$. Transmission electron microscopy (TEM) image of the intermediate sample prepared with Ag nanoparticles, ethanol, 20% water and BiOCl via hydrothermal method is demonstrated in Figure S10, Supporting Information, to further claim the role of Ag nanoparticles. It can be observed that Ag nanoparticles, BiOCl, and Bi_2O_3 exist simultaneously. Besides, Bi_2O_3 nanosheets are formed at the position where Ag nanoparticles are present. For the position where there are no Ag nanoparticles, no Bi_2O_3 nanosheets
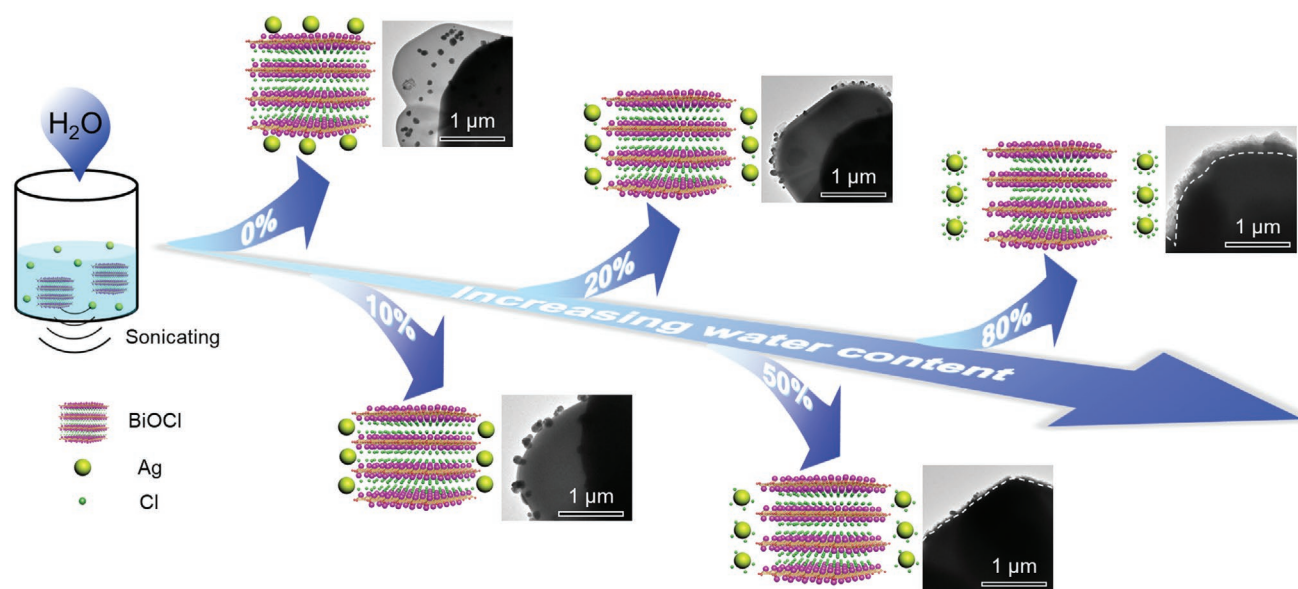

Figure 1. Schematic illustration of the fabrication process of lateral heterogeneous $BiOCl@Bi_2O_3$.

are present and BiOCl nanoplate keeps the original sharp edge. It further confirms the role of Ag during the fabrication of $BiOCl@Bi_2O_3$. Thus, it can be concluded that both water and Ag are indispensable components in fabricating 2D lateral heterogeneous $BiOCl@Bi_2O_3$. In this work, $BiOCl@Bi_2O_3$ prepared with 80% of water is selected to characterize its structure and CO_2 photoreduction performance.

X-ray diffraction (XRD) analysis was adopted to characterize the composition of the as-prepared powders. As shown in **Figure 2**a, the diffraction peaks in the XRD pattern can be indexed to BiOCl and Bi_2O_3, indicating that the as-synthesized materials mainly contain BiOCl and Bi_2O_3 components. The annular dark-field TEM in Figure 2b and low-resolution TEM image of single particle in Figure S11, Supporting Information, demonstrate that there is a clear brightness contrast between the middle and edge part of the as-prepared particle. The top view (Figure S12, Supporting Information) and cross-sectional (Figure S13, Supporting Information) SEM images of the as-prepared particles further confirm the existence of the interface

between edge part and middle part in the as-prepared particles. By characterizing the atomic high-resolution TEM image on the heterointerface, it can be observed in Figure 2c that there is no big difference in the lattice fringe between the middle and edge part of the as-prepared particle, revealing that the fabrication method in this work will not change the lattice assignment at the heterointerface and thus perfect lateral epitaxial heterostructure can be generated. To further confirm the composition of the middle and edge part of the as-prepared particle, the EDS elemental mapping and EDS line profiles were carried out on Bi, O, and Cl atoms, and the corresponding results are illustrated in Figure 2d–f. It is clear that Bi has a large distribution both in the middle and the edge part, and O has a smaller distribution in the middle part and a large distribution in the edge part. In contrast, Cl has a large distribution in the middle part and a negligible distribution in the edge part. Combining with XRD analysis, it can be concluded that the middle component of the as-prepared particle is BiOCl and the edge component is Bi_2O_3, suggesting that Cl in the edge part of BiOCl has been
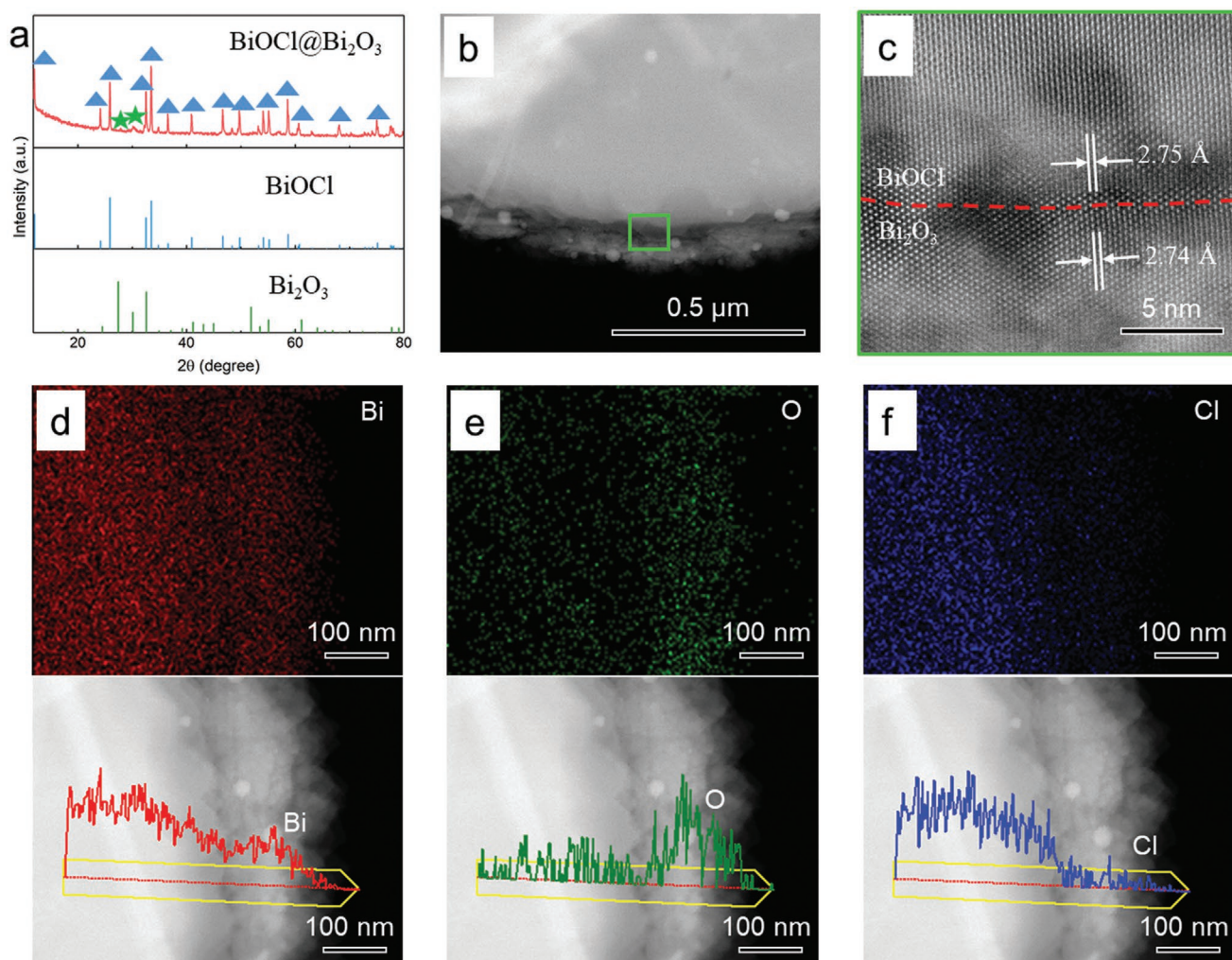
Figure 2. a) XRD pattern of the as-prepared $BiOCl@Bi_2O_3$. The standard patterns of BiOCl with JCPDS No. 82–0485 and Bi2O3 with JCPDS No. 45–1344 have also been displayed. b) The annular dark-field image of $BiOCl@Bi_2O_3$. c) The atomic high-resolution TEM image of $BiOCl@Bi_2O_3$ for the selected area marked with green box in (b). The boundary between BiOCl and Bi_2O_3 are marked by red dashes. d–f) The EDS elemental mappings and line profiles for Bi, O, and Cl, respectively.

**ADVANCED
SCIENCE NEWS**

www.advancedsciencenews.com

**ADVANCED
MATERIALS**

www.advmat.de

etched out with the assistance of water and noble metal particle without distorting the lattice at the heterointerface. It reveals that etching facilitates the growth of epitaxial heterostructure via removing the elements between layers in the 2D layered materials.

X-ray photoelectron spectroscopic (XPS) analysis was employed to further study the chemical composition of the as-prepared lateral heterostructure. As shown in Figure S14, Supporting Information, there are three deconvolved peaks in the high-resolution core-level XPS spectrum of O 1s for $BiOCl@Bi_2O_3$, which is quite different from pure BiOCl which only presents two deconvolved peaks in the XPS spectra. The peak observed at 530.15 eV for BiOCl and 529.84 eV for $BiOCl@Bi_2O_3$ are assigned to the lattice oxygen.[22,23] Since Cl atom in the edge of BiOCl is etched out in $BiOCl@Bi_2O_3$, the concentration of the positive charges on Bi atom in $BiOCl@Bi_2O_3$ at the edge part is decreased. As a result, the electron screening effect for the related Bi-O bonding is decreased,[24,25] which results in decreased bonding energy for lattice oxygen in $BiOCl@Bi_2O_3$. Similar phenomenon appears in the bridging hydroxyls with XPS peak sited at 531.97 eV for BiOCl and 530.61 eV for $BiOCl@Bi_2O_3$. Compared with BiOCl, XPS spectra of O 1s for $BiOCl@Bi_2O_3$ presents another additional peak shoulder located at 533.52 eV which belongs to the physisorbed water.[26] This is attributed to the fact that the open metal sites caused by etching of interlayer Cl in $BiOCl@Bi_2O_3$ have strong interaction with the surrounding water.
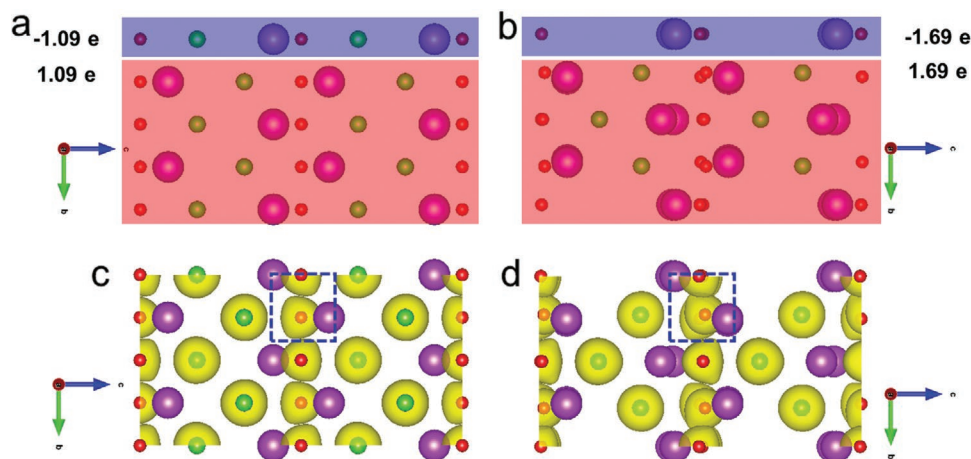
Figure 3a shows the UV–vis diffuse reflectance spectra of the as-prepared BiOCl and $BiOCl@Bi_2O_3$. It can be observed that BiOCl possesses a featured absorption band with the edge at about 370 nm.[4] In contrast, there are two absorption bands

in the UV–vis diffuse reflectance spectrum of $BiOCl@Bi_2O_3$. The one with the edge at about 370 nm is assigned to band-gap absorption of BiOCl, and another one with the edge extended to 613 nm belonged to Bi_2O_3. It is obvious that there is no big difference on the band-gap absorption of BiOCl for pure BiOCl and $BiOCl@Bi_2O_3$, indicating that the etching assisted growth of lateral heterostructure do not change much on the original 2D materials. Potentiostatic electrochemical impedance spectrum (PEIS) measurement is generally employed to evaluate interface resistance and carrier mobility of semiconductors.[21] As demonstrated in Figure 3b, the impedance radius of $BiOCl@Bi_2O_3$ is much smaller than that of BiOCl, revealing that the resistance for the charge transfer in $BiOCl@Bi_2O_3$ is lower than that in BiOCl. Thus, compared with BiOCl, the photogenerated charge carriers in $BiOCl@Bi_2O_3$ possess larger mobility, which facilitates the photocatalytic process.

Transient pump-proble absorption spectroscopy (TAS) is a well-known technique in developing in-depth understanding of photoexcited charge carrier dynamics and interfacial charge transfer dynamics.[27–29] The TAS spectrum of BiOCl in Figure S15, Supporting Information, and TAS spectrum of $BiOCl@Bi_2O_3$ in Figure 3c show a featured bleaching peak at around 390 nm which is assigned to state-filling effect of the band edge of BiOCl.[30,31] Besides, a positive signal sited at about 380 nm is observed in $BiOCl@Bi_2O_3$ and it is arising from electroabsorptive effects of Bi_2O_3. The electron lifetime in $BiOCl@Bi_2O_3$ probed by TAS kinetics (Figure 3d) is observed to be a little longer than that in BiOCl. It reveals the existence of charge-separation states in $BiOCl@Bi_2O_3$ which is originated from internal electric field induced by strong chemical bonding at the heterointerface.[31] To further confirm it, we
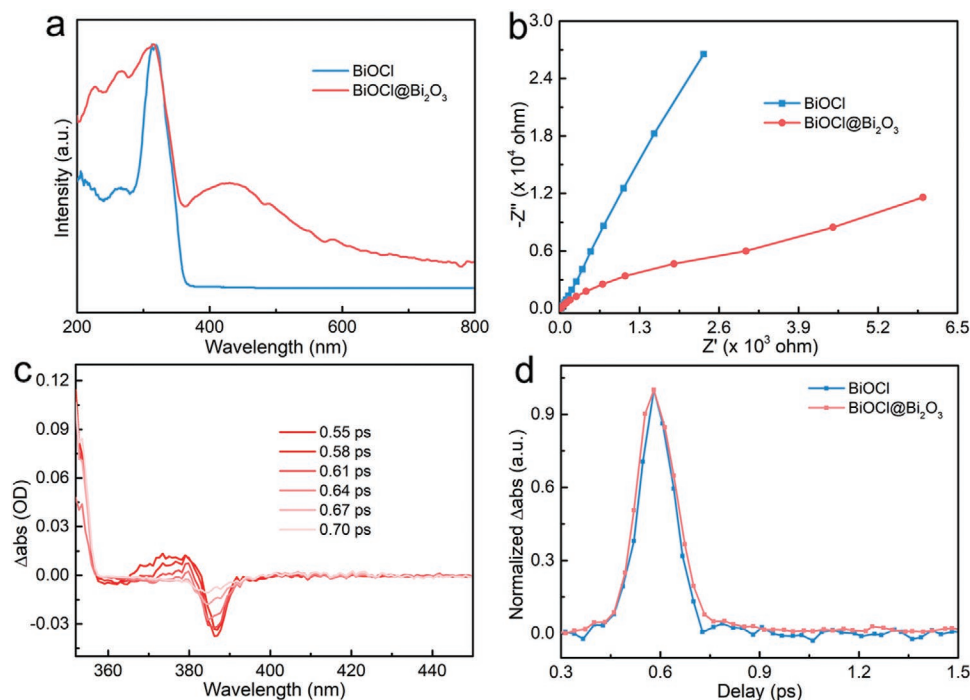
Figure 3. a) UV–vis diffuse reflectance spectra of BiOCl and $BiOCl@Bi_2O_3$. b) The PEIS spectra of BiOCl and $BiOCl@Bi_2O_3$. c) TAS spectra of $BiOCl@Bi_2O_3$ at indicated delay with the excitation pump of 350 nm and excitation power density of 6 μJ cm^{-2}. d) TAS kinetics probed at around 390 nm for BiOCl and $BiOCl@Bi_2O_3$.

**ADVANCED
SCIENCE NEWS**

www.advancedsciencenews.com

**ADVANCED
MATERIALS**

www.advmat.de

Figure 4. a) Crystal structure of BiOCl viewed from the [001] direction with Bader charge analysis results marked. b) Crystal structure of BiOCl@Bi_2O_3 viewed from the [001] direction with Bader charge analysis results marked. c) Charge density distribution of BiOCl. d) Charge density distribution of BiOCl@Bi_2O_3.

carried out DFT simulation on BiOCl and BiOCl@Bi_2O_3. As shown in **Figure 4**a,b, the charge amount for the edge and centre part in BiOCl@Bi_2O_3 is about 1.69 eV, which is larger than that in BiOCl, indicating a stronger chemical bonding in BiOCl@Bi_2O_3 when Cl in the edge part is etched out. Similar phenomenon can be observed in electron density distribution. Figure 4c,d demonstrate that compared with BiOCl, the electron density distribution of O in [Bi_2O_2]$^{2+}$ slab of BiOCl@Bi_2O_3 at the heterointerface is more prone to be directed to the edge part. It suggests a stronger chemical bonding in BiOCl@Bi_2O_3, this stronger chemical bonding induces the generation of stronger internal electric field which contributes to better photoexcited charge separation and charge transfer kinetics.

Benefiting from better charge separation and charge transfer kinetics, BiOCl@Bi_2O_3 is proposed to be able to generate more photoexcited charge carriers. Transient photocurrent response is a direct way to check the amount of photoexcited charge carriers. With larger amount of photoexcited charge carriers, the intensity of the photocurrent is higher. The results of transient photocurrent response over BiOCl@Bi_2O_3 and BiOCl under simulated solar light are displayed in Figure S16, Supporting Information. The current density of BiOCl@Bi_2O_3 in each light-on cycle is about −1.05 μA cm^{-2}, which is 7 times that of BiOCl. In contrast, for BiOCl@Bi_2O_3 with vertical heterostructure reported in reference,[32] the current density is about 0.70 μA cm^{-2} which is less than 5 times that of pure BiOCl, indicating that lateral heterostructure is superior than vertical heterostructure. Thus, it can be documented that strong internal electric field at the lateral epitaxial heterojunction of BiOCl@Bi_2O_3 can help to facilitate more efficient photoexcited charge separation and generate more photoinduced charge carriers.

The detection of molecular oxygen active species is another effective way to check the species and amount of photoexcited charge carriers. Generally, •OH is employed to evaluate positive charge carriers and •O_2^- is employed to evaluate negative charge carriers. DMPO assisted ESR measurement can be used to detect molecular oxygen active species.[33,34] As shown in **Figure 5**a, both BiOCl and BiOCl@Bi_2O_3 present four ESR signals with the intensities of 1:2:2:1 under simulated solar light, which is contributed to the appearance of DMPO-•OH adduct originated from the OH$^-$/H_2O oxidation by holes.[23] Compared with BiOCl, the ESR signals of BiOCl@Bi_2O_3 is stronger. As the square of signal intensity is approximately proportional to the number of free radicals,[35] more charge carriers can be generated over BiOCl@Bi_2O_3 under simulated solar light illumination. Similar phenomenon can be observed in Figure 5b, in which four ESR signals assigned to DMPO-•O_2^- and related with the O_2 reduction by electrons can be detected.[36] Hence, it can be inferred that BiOCl@Bi_2O_3 can produce larger number of holes and electrons under simulated solar light in the photocatalytic process. Figure 5c shows that no ESR signals can be detected over pure BiOCl under visible light irradiation whereas four peaks of DMPO-•OH are observed over BiOCl@Bi_2O_3 in the same process. The inspection of DMPO-•O_2^- in Figure 5d demonstrates that both BiOCl and BiOCl@Bi_2O_3 cannot produce electrons under visible light irradiation. Thus, it is obvious that the introduction of Bi_2O_3 can facilitate BiOCl@Bi_2O_3 to utilize the visible light to produce holes. Since Ag nanoparticles are employed in assisting the growth of BiOCl@Bi_2O_3, we compared the visible-light-driven oxygen active species of BiOCl@Bi_2O_3 and BiOCl-Ag to further check whether BiOCl@Bi_2O_3 is influenced by the plasmonic effect induced by residual Ag. The results are demonstrated in Figure S17, Supporting Information. It is clear that the visible-light-driven oxygen active species in BiOCl@Bi_2O_3 and BiOCl-Ag are completely different. The visible-light-driven oxygen active species in BiOCl@Bi_2O_3 are mainly •OH while those in BiOCl-Ag are mainly •O_2^-, revealing that the plasmonic effect induced by few amounts of residual Ag has negligible influence on BiOCl@Bi_2O_3, and the outstanding photocatalytic activity of BiOCl@Bi_2O_3 is mainly originated from the construction of lateral heterostructures.

CO_2 photoreduction was carried out to further investigate the role of the lateral heterojunction in the application of lateral heterogeneous BiOCl@Bi_2O_3. As shown in **Figure 6**a, the CO yield rate of BiOCl@Bi_2O_3 is about 75 μmol g^{-1} h^{-1} under simulated solar light while the CO yield rate of BiOCl is about
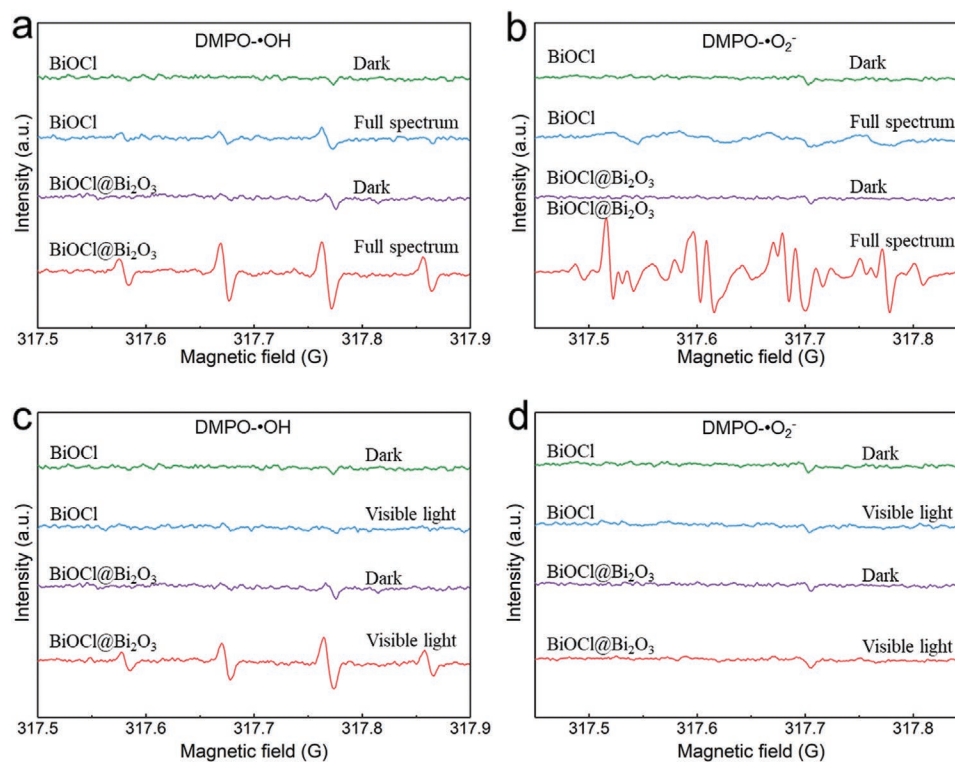
Figure 5. a,b) ESR signals for DMPO-•OH (a) and DMPO-•O_2^- (b) over BiOCl and BiOCl@Bi_2O_3 under simulated solar light irradiation for 4 min. c,d) ESR signals for DMPO-•OH (c) and DMPO-•O_2^- (d) over BiOCl and BiOCl@Bi_2O_3 under visible light ($\lambda > 420$ nm) irradiation for 4 min.

52 µmol g^{-1} h^{-1} under same conditions. With the irradiation of visible light, nearly no CO is generated by BiOCl, indicating that pure BiOCl cannot utilize visible light to reduce CO_2 into fuel energy. In contrast, a CO yield rate of about 29 µmol g^{-1} h^{-1} can be observed over BiOCl@Bi_2O_3 in the same process. The rather larger CO yield over BiOCl@Bi_2O_3 under visible light benefits from the visible absorption of Bi_2O_3 and the superior charge separation driven by the intrinsic electric field induced by the lateral heterojunction. The details of the CO_2 photoreduction process is studied via inspecting the time-dependent CO yield. Figure 6c shows that the yield of CO increases smoothly with the increasing of irradiation time under visible light illumination, and about 386 µmol g^{-1} can be generated over BiOCl@Bi_2O_3 in 12 h. Figure 6d presents three cycling test of the CO_2 photoreduction process under the irradiation of visible light. It can be observed that the CO yield rate in each test time is stable and all the values are around 30 µmol g^{-1} h^{-1}, indicating that the photoreduction properties over BiOCl@Bi_2O_3 is stable. Isotope measurement with $^{13}CO_2$ as the source was carried out to check whether the yield of CO is originated from the photoreduction of CO_2 instead of atmosphere or other sources.[30] Figure 6e demonstrates that the ^{13}CO is the mainly product in the photocatalytic process, revealing that the CO is indeed generated by the photoreduction of CO_2.

In summary, the lateral heterogeneous BiOCl@Bi_2O_3 2D material was prepared via etching with the assistance of noble-metal nanoparticles and water under sonicating. Benefiting from the strong intrinsic electric field induced by chemical bonding at the lateral heterointerface, BiOCl@Bi_2O_3 possesses outstanding charge separation and mobility properties. In addition, Bi_2O_3 can utilize visible light. Due to these multiple advantages, the CO_2 photoreduction properties of BiOCl@Bi_2O_3 is enhanced in a large extent and the visible-light-driven CO yield rate is about 30 µmol g^{-1} h^{-1}. The method to fabricate lateral heterostructure in this work can help to enrich the current family of 2D heterogeneous materials, and thus will promote the applications of these 2D materials in optical devices, energy conversion, and storage fields.

Experimental Section

Chemicals: Sodium chloride (NaCl, 99.5%), bismuth (III) nitrate pentahydrate (Bi(NO$_3$)$_3\cdot$5H$_2$O, 99.999%), polyvinylpyrrolidone (PVP, Mw ≈ 40 000), silver nitrate (AgNO$_3$, 99.0%), and hydrazine hydrate (NH$_2$NH$_2\cdot$H$_2$O, 50–60%) were purchased from Sigma-Aldrich. Ethanol (C$_2$H$_5$OH, 100%) was purchased from Chem-Supply Pty. Ltd. All chemicals were used as received without further purification.

Synthesis of BiOCl: First, 0.058 g NaCl were dissolved into 15 mL distilled water containing 0.486 g Bi(NO$_3$)$_3\cdot$5H$_2$O under vigorous stirring for 30 min. Second, the suspension was transferred to a 50 mL Teflon-lined stainless-steel autoclave, and then heated at 170 °C for 16 h. Finally, the products were washed with distilled water and ethanol, and then dried at 80 °C for 24 h in air.

Synthesis of Ag Nanosphere: 100 mg AgNO$_3$ were added into 20 mL-glass vial containing 2 mL 10 mg mL^{-1} PVP aqueous solution. After magnetic stirring for 5 min, 2 µL hydrazine hydrate solution was slowly dropped into the above mixture. The reduction reaction was carried out at room temperature for 2 min with continuous magnetic stirring. Then the resulting products were collected via centrifugation and washed with 100% ethanol for several times. The final Ag nanoparticles with the size
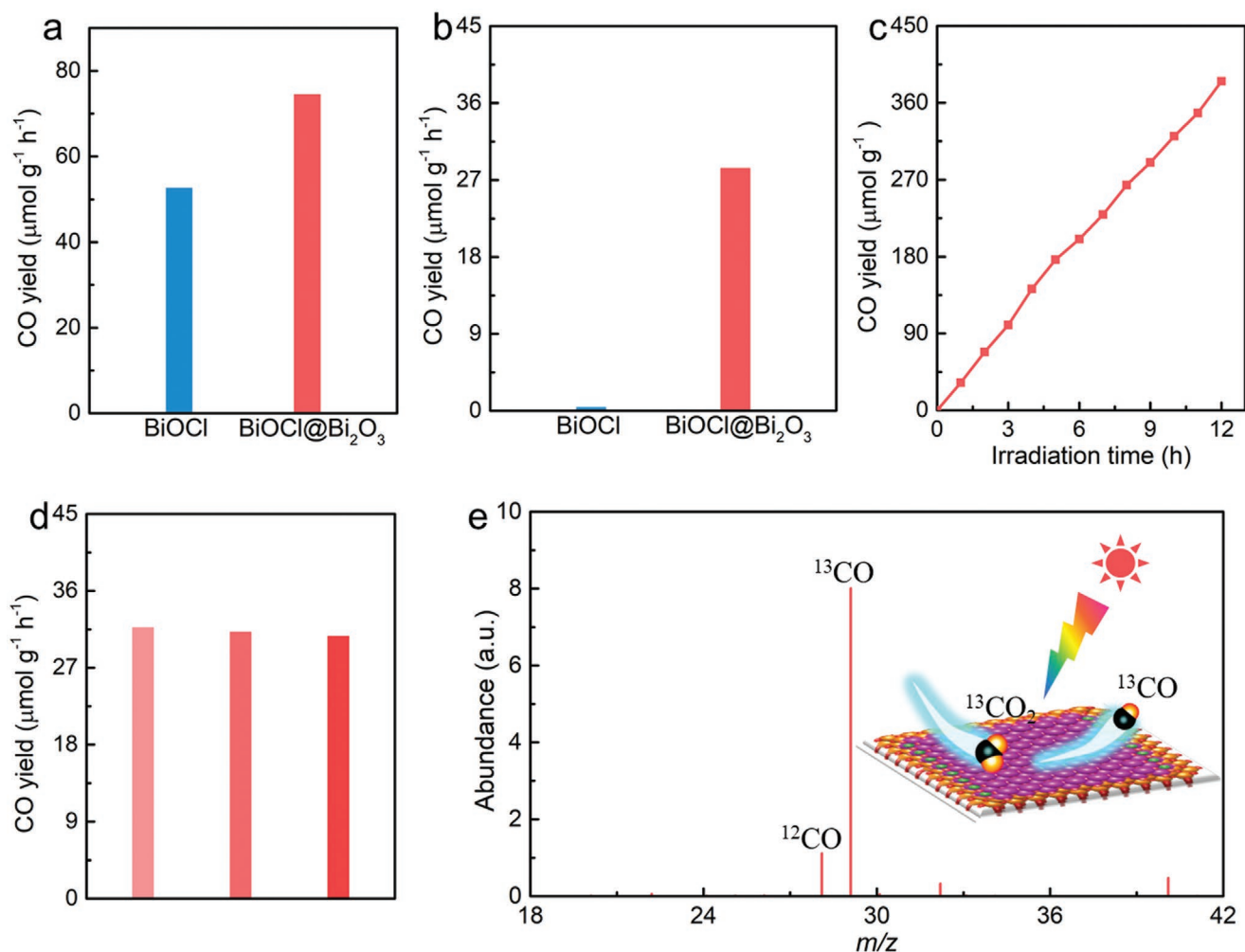
Figure 6. a,b) CO yield rate of photoreduction of CO_2 over BiOCl and BiOCl@Bi_2O_3 under simulated solar light (a) and visible light ($\lambda > 420$ nm) (b). c) Time-dependent photoreduction of CO_2 over BiOCl@Bi_2O_3 under visible-light irradiation. d) The cycling test of photoreduction of CO_2 over BiOCl@Bi_2O_3 under the illumination of visible light. e) Isotope measurement for the CO_2 photoreduction process over BiOCl@Bi_2O_3 under visible light irradiation.

selected by centrifugation at 3100 rpm for 2 min were redispersed into 2 mL 100% ethanol.

Synthesis of BiOCl@Bi_2O_3: 10 mg BiOCl nanoplates were dispersed into 40 mL solvent containing 32 mL distilled water and 8 mL 100% ethanol. Then 0.5 mL 5 mg mL^{-1} Ag aqueous solution was dropped into the above suspension under ultrasonication. After 5 min, the mixture was transferred to a 50 mL Teflon-lined stainless-steel autoclave and then heated at 100 °C for 1 h. The final product was collected and washed with ethanol for several times, and then dried at 60 °C for 24 h.

Characterizations: The XRD pattern of the as-synthesized sample was collected by GBC MMA X-ray powder diffractometer with Cu-Kα1 radiation (40 kV, 25 mA, $\lambda = 0.15\,418$ nm). JEOL JSM-7500 was used to obtain the scanning electron microscopy images, and the JEOL JEM-2010 was used to acquire the typical TEM images. The high-resolution TEM images and the EDS elemental mappings were conducted by JEOL ARM-200F under the voltage of 200 kV. Shimadzu UV-3600 was employed to characterize the UV–vis diffuse reflectance spectra. The photoelectron spectroscopy station (Beamline 4W9B) with the resolution of 0.05 eV was adopted to obtain the high-resolution X-ray photoelectron spectroscopy spectrum. The detection of the active oxygen species was carried out by the JES-FA200 ESR Spectrometer.

VSP-300 electrochemical analyzer with standard three-electrode set-up was used to conduct the photoelectrochemical characterization.

A platinum foil, Ag/AgCl electrode and 0.5 M Na_2SO_4 were selected as the counter electrode, reference electrode, and the electrolyte, respectively. The working electrode was prepared by depositing the as-synthesized powders on the glassy carbon electrode. 300 W Xe lamp with the distance of 10 cm to the working electrode was employed as the light source to test the photocurrent response. The PEIS was tested in the frequency range of 100 mHz to 200 kHz, and the Mott–Schottky measurements was carried out at the fixed frequency of 1 kHz.

A reaction cell, in which 3 mL distilled water was added and a quartz fiber filter with 50 mg photocatalyst uniformly deposited was placed and was adopted to characterize the photoreduction of CO_2 under an atmospheric pressure of CO_2. The 300 W Xe lamp with 420 nm cut-off filter was selected to simulate the visible light. A gas chromatography equipped with a packed molecular sieve column (TDX-01 mesh) was employed to detect the produced gas. The isotropic test was conducted under same conditions with the above experiment except $^{13}CO_2$ selected as the carbon source. Gas chromatography–mass spectrometry was used to carry out the detection of CO in the isotropic measurement.

Pump–probe TAS measurement was performed by adopting a regenerative amplified Ti:sapphire laser system with the coherent wavelength of 800 nm. The pump light was generated by employing optical prametric amplifier to generate a laser pulse with the wavelength of 350 nm. The probe light was generated via employing a CaF$_2$ window

to attenuate the 800 nm output beam. The samples were dispersed into water and then placed in 1 nm quarts cuvettes for measurement. The absorption intensity of the samples in 1 nm quarts cuvettes should be about 0.1 OD.

All theoretical simulations were carried by employing Vienna Ab initio Simulation Package (VASP) with Perdew–Burke–Ernzehof as the functional. The k-point mesh for the simulated samples is set as $7 \times 7 \times 7$. The convergence energy threshold for the optimization of the simulation process is set as 1×10^{-6} eV.

Supporting Information

Supporting Information is available from the Wiley Online Library or from the author.

Acknowledgements

Conflict of Interest

The authors declare no conflict of interest.

Keywords

[1] Y. Qu, X. Duan, *Chem. Soc. Rev.* **2013**, *42*, 2568.

[2] L. Wang, X. Xu, Q. Cheng, S. X. Dou, Y. Du, *Small* https://doi.org/10.1002/smll.201904107.

[3] D. Ginley, M. A. Green, R. Collins, *MRS Bull.* **2011**, *33*, 355.

[4] L. Wang, D. Lv, Z. Yue, H. Zhu, L. Wang, D. Wang, X. Xu, W. Hao, S. X. Dou, Y. Du, *Nano Energy* **2019**, *57*, 398.

[5] A. Kudo, Y. Miseki, *Chem. Soc. Rev.* **2009**, *38*, 253.

[6] X. Wang, K. Maeda, A. Thomas, K. Takanabe, G. Xin, J. M. Carlsson, K. Domen, M. Antonietti, *Nat. Mater.* **2009**, *8*, 76.

[7] X. Chen, S. Shen, L. Guo, S. S. Mao, *Chem. Rev.* **2010**, *110*, 6503.

[8] W. Che, W. Cheng, T. Yao, F. Tang, W. Liu, H. Su, Y. Huang, Q. Liu, J. Liu, F. Hu, Z. Pan, Z. Sun, S. Wei, *J. Am. Chem. Soc.* **2017**, *139*, 3021.

[9] N. Jiang, B. You, M. Sheng, Y. Sun, *ChemCatChem* **2016**, *8*, 106.

[10] Y. Gong, J. Lin, X. Wang, G. Shi, S. Lei, Z. Lin, X. Zou, G. Ye, R. Vajtai, B. I. Yakobson, H. Terrones, M. Terrones, B. K. Tay, J. Lou, S. T. Pantelides, Z. Liu, W. Zhou, P. M. Ajayan, *Nat. Mater.* **2014**, *13*, 1135.

[11] Y. Dou, L. Zhang, X. Xu, Z. Sun, T. Liao, S. X. Dou, *Chem. Soc. Rev.* **2017**, *46*, 7338.

[12] M. Guan, C. Xiao, J. Zhang, S. Fan, R. An, Q. Cheng, J. Xie, M. Zhou, B. Ye, Y. Xie, *J. Am. Chem. Soc.* **2013**, *135*, 10411.

[13] X. Huang, Z. Zeng, H. Zhang, *Chem. Soc. Rev.* **2013**, *42*, 1934.

[14] Q. H. Wang, K. Kalantar-Zadeh, A. Kis, J. N. Coleman, M. S. Strano, *Nat. Nanotechnol.* **2012**, *7*, 699.

[15] A. K. Geim, I. V. Grigorieva, *Nature* **2013**, *499*, 419.

[16] B. W. H. Baugher, H. O. H. Churchill, Y. Yang, P. Jarillo-Herrero, *Nat. Nanotechnol.* **2014**, *9*, 262.

[17] Y. Zhang, T. Mori, L. Niu, J. Ye, *Energy Environ. Sci.* **2011**, *4*, 4517.

[18] Y. Hou, A. B. Laursen, J. Zhang, G. Zhang, Y. Zhu, X. Wang, S. Dahl, I. Chorkendorff, *Angew. Chem., Int. Ed.* **2013**, *52*, 3621.

[19] L. Wang, D. Lv, F. Dong, X. Wu, N. Cheng, J. Scott, X. Xu, W. Hao, Y. Du, *ACS Sustainable Chem. Eng.* **2019**, *7*, 3010.

[20] L. Ye, L. Zan, L. Tian, T. Peng, J. Zhang, *Chem. Commun.* **2011**, *47*, 6951.

[21] X. Wu, Y. H. Ng, L. Wang, Y. Du, S. X. Dou, R. Amal, J. Scott, *J. Mater. Chem. A* **2017**, *5*, 8117.

[22] H. Huang, K. Liu, K. Chen, Y. Zhang, Y. Zhang, S. Wang, *J. Phys. Chem. C* **2014**, *118*, 14379.

[23] Y. Zhou, Y. Zhang, M. Lin, J. Long, Z. Zhang, H. Lin, J. C. S. Wu, X. Wang, *Nat. Commun.* **2015**, *6*, 8340.

[24] X. Liu, Y. Su, Q. Zhao, C. Du, Z. Liu, *Sci. Rep.* **2016**, *6*, 28689.

[25] X. H. Li, H. Y. Xu, X. T. Zhang, Y. C. Liu, J. W. Sun, Y. M. Lu, *Appl. Phys. Lett.* **2009**, *673*, 95.

[26] L. Li, J. Yan, T. Wang, Z.-J. Zhao, J. Zhang, J. Gong, N. Guan, *Nat. Commun.* **2015**, *6*, 5881.

[27] R. Godin, Y. Wang, M. A. Zwijnenburg, J. Tang, J. R. Durrant, *J. Am. Chem. Soc.* **2017**, *139*, 5216.

[28] P. Wang, Y. Mao, L. Li, Z. Shen, X. Luo, K. Wu, P. An, H. Wang, L. Su, Y. Li, S. Zhan, *Angew. Chem., Int. Ed.* **2019**, *58*, 11329.

[29] B. C. M. Martindale, G. A. M. Hutton, C. A. Caputo, S. Prantl, R. Godin, J. R. Durrant, E. Reisner, *Angew. Chem., Int. Ed.* **2017**, *56*, 6459.

[30] K. Wu, Z. Chen, H. Lv, H. Zhu, C. L. Hill, T. Lian, *J. Am. Chem. Soc.* **2014**, *136*, 7708.

[31] K. Wu, H. Zhu, Z. Liu, W. Rodríguez-Córdoba, T. Lian, *J. Am. Chem. Soc.* **2012**, *134*, 10337.

[32] X. Tang, C. Ma, N. Liu, C. Liu, S. Liu, *Chem. Phys. Lett.* **2018**, *709*, 82.

[33] H. Huang, X. Li, J. Wang, F. Dong, P. K. Chu, T. Zhang, Y. Zhang, *ACS Catal.* **2015**, *5*, 4094.

[34] H. Huang, S. Tu, C. Zeng, T. Zhang, A. H. Reshak, Y. Zhang, *Angew. Chem., Int. Ed.* **2017**, *56*, 11860.

[35] Y. Li, S. Ouyang, H. Xu, X. Wang, Y. Bi, Y. Zhang, J. Ye, *J. Am. Chem. Soc.* **2016**, *138*, 13289.

[36] S. Weng, Z. Pei, Z. Zheng, J. Hu, P. Liu, *ACS Appl. Mater. Interfaces* **2013**, *5*, 12380.